Can the mechanoreceptional setae of a feeding-current feeding copepod detect hydrodynamic disturbance induced by entrained free-floating prey?

Shen, Xinhui; Yao, Xin; Marcos; Fu, Henry C.

2021

Shen, X., Yao, X., Marcos & Fu, H. C. (2021). Can the mechanoreceptional setae of a feeding-current feeding copepod detect hydrodynamic disturbance induced by entrained free-floating prey?. Limnology and Oceanography, 66(12), 4096-4111. https://dx.doi.org/10.1002/lno.11945

https://hdl.handle.net/10356/153648

https://doi.org/10.1002/lno.11945

Supplemental Information -- Can the mechanoreceptional setae of a feeding-current feeding copepod detect hydrodynamic disturbance induced by entrained free-floating prey?

Xinhui Shen[1], Xin Yao[1], Marcos[1*], Henry C. Fu[2*]

[1] School of Mechanical and Aerospace Engineering, Nanyang Technological University, Singapore

[2] Department of Mechanical Engineering, University of Utah, Salt Lake City, Utah 84112, USA

ORCID ID for Marcos: https://orcid.org/0000-0001-5657-196X

ORCID ID for Henry C. Fu: https://orcid.org/0000-0002-3543-7128

* Correspondence: marcos@ntu.edu.sg, henry.fu@utah.edu

Running head: Prey detection in feeding currents

Key Words: copepods, seta, mechanoreception, feeding-current feeding, prey detection, hydrodynamic sensitivity, setal deformation

Detailed copepod model

The geometry of our copepod model is based on copepods *Paracalanus parvus* and *Pseudocalanus sp.* in supplementary videos 1 and 3 of Tiselius et al. (2013). The copepod prosome of length L_b = 1 mm is approximated to be two semi-ellipsoids attached to a cone-shaped urosome; the cephalosome is then extruded to allow the attachment of the cephalic appendages (Fig. S1). The stationary swimming legs are modeled as a prism intersecting with the prosome, while the centerline of the antennule with arc length L_{A1} = 1.097 mm is fitted to a fifth-order polynomial. Figs. S1a,b show the geometrical parameters of the copepod model.

The feeding appendage geometries and beating patterns are modeled as follows. Morphological examination shows that the antennae, first maxillae, and mandibles are biramous (two branches) while the maxillipeds are uniramous (single branch); the distal segments of mandibles share a common proximal segment and are separated by a small angle (refer to fig. 2 of Conway (2006)). We first determine the attachment points of appendage roots from Tiselius et al. (2013), which are represented by the longitudinal distance measured from the head tip l and lateral distance from the sagittal plane w (refer to Fig. S1a insert, and also see the "l" and "w" columns in Table S1). To model the appendage geometries, we then approximate the first maxilla to be a cylinder with one degree of freedom only (see Fig. S1c). The distal segments of the mandible are close to each other, so we treat them as one branch. Therefore, we approximate each branch of antenna, mandible and maxilliped as a rigid circular frustum (see the "root diameter" column in Table S1). The setules and setae on the feeding appendages are not explicitly accounted for in the hydrodynamic model; instead, the root diameters of all appendages are 1.5 times the values obtained from the image analysis.

We obtain the projected motions of the antennae, mandibles, first maxillae and maxillipeds from supporting video 1 of Tiselius et al. (2013), as these four pairs of appendages are involved in generating the actual feeding current (Tiselius et al. 2013; van Duren and Videler 2003). For each appendage, in every video frame we determine the angles from the copepod's transverse plane to the proximal and distal segments, θ_1 and θ_2 (see Fig. S1a inset), respectively. We perform a fast Fourier transform on all θ_1 and θ_2 to express their time-dependence analytically by using the first two leading terms (see the "angle" column in Table S1). The last pair of feeding appendages, second maxillae, is found to stay almost stationary (Gill and Poulet 1986) and only move occasionally to handle food particles upon detection (van Duren and Videler 2003); therefore, we neglect the presence of the second maxillae in our model.

To recover the three dimensional beating patterns of the feeding appendages, we find the mean projected lengths of the four feeding appendages, antennae, mandibles, first maxillae, and maxillipeds, from supporting video 1 of Tiselius et al. (2013), and the corresponding projection angle α in Fig. S1a inset, according to the copepod schematics as shown in fig. 2 of Koehl and Strickler (1981). Table S1 shows the true lengths and α of all feeding appendage segments.

Immersed boundary method

Governing equations

The feeding current and prey entrainment are governed by the unsteady and incompressible Navier-Stokes equations

$$\rho\left[\partial_t \mathbf{u}(\mathbf{x},t)+\mathbf{u}(\mathbf{x},t)\cdot\nabla\mathbf{u}(\mathbf{x},t)\right]=-\nabla p(\mathbf{x},t)+\mu\nabla^2\mathbf{u}(\mathbf{x},t)+\mathbf{f}_b(\mathbf{x},t), \tag{S1}$$

$$\nabla\cdot\mathbf{u}(\mathbf{x},t)=0, \tag{S2}$$

where $\rho = 10^3$ kg/m^3 is the fluid density; $\mu = 10^{-3}$ Ns/m^2 is the viscosity; $\mathbf{u}$, p, $\mathbf{f}_b$ are the fluid velocity, pressure, and force at position $\mathbf{x}$ and time t, respectively.

Due to the no-slip boundary condition, the fluid velocity at the surfaces of the copepod and its appendages must be equal to the velocity of those surfaces. Owing to the complexity of the feeding appendages' beating strokes, it is useful to apply the immersed boundary (IB) method to account for the no-slip boundary condition (Peskin 1972; Peskin 2002), which requires forces to be exerted on the fluid at the surfaces. The forces and the no-slip boundary condition in the IB framework are expressed as

$$\mathbf{f}_b(\mathbf{x},t) = \int_U \mathbf{F}(\mathbf{s},t)\,\delta\big(\mathbf{x}-\mathbf{X}(\mathbf{s},t)\big)\,d\mathbf{s}, \tag{S3}$$

$$\partial_t \mathbf{X}(\mathbf{s},t) = \int_\Omega \mathbf{u}(\mathbf{x},t)\,\delta\big(\mathbf{x}-\mathbf{X}(\mathbf{s},t)\big)\,d\mathbf{x}, \tag{S4}$$

where Ω denotes the space occupied by the immersed copepod; $\mathbf{F}(\mathbf{s},t)$ and $\mathbf{X}(\mathbf{s},t)$ are the force density applied by the copepod to the fluid and its physical position of the material point $\mathbf{s} \in \Omega$ at time t, respectively; $\delta(\mathbf{x})$ is the three-dimensional Dirac delta function in our problem.

Mesh independence test

The spatial and temporal distribution of the feeding current due to a tethered feeding-current feeding copepod is calculated by using the constraint IB version (Bhalla et al. 2013) of IBAMR (https://ibamr.github.io/, last accessed on July 23, 2021). In our simulation, we set the origin of the Cartesian coordinate to be at the center of a cubical computational domain of length L = 10 mm. We then place the copepod of prosome length L_b = 1 mm into the domain such that at time t = 0, the copepod's center of mass coincides with the origin, its anterior-posterior direction along the positive x-axis and its ventral-dorsal direction along the positive z-axis. IBAMR discretizes the computational domain into Cartesian grids and refines the grids if necessary. As a result, the coarsest grids are distributed around the boundaries of the computational domain, while the finest grids enclose the tethered copepod and prey. There are three variables that determine the

total number of grids: first, the number of coarsest grids per length N which controls the size of the coarsest grid $dx^1 = L/N$, second, the refinement ratio R_{ref}^i which controls how each coarse grid is divided into the next finer grid with size $dx^{i+1} = dx^i / R_{\text{ref}}^i$, and last, the refinement level n_{ref}, which determines the upper bound of the positive integer i. The mesh refinement is automatically determined by the IBAMR software, and hence the grid may vary between each time step.

The mesh independence test is performed by comparing the velocities at three sample points in the computational domain as the variables $(N, R_{\text{ref}}^i, n_{\text{ref}})$ are varied: the tips of the proximal and distal setae on the left antennule, and Point D close to the beating appendages at $\mathbf{x}/L_{\text{b}} = [0, 0, -0.5]$. The mesh independence test is conducted by setting the maximum time step $\Delta t_{\text{max}}/T = 5 \times 10^{-4}$ so that the convective Courant-Friedrichs-Lewy number is not more than 0.05, where the period of the beating stroke $T = 1/30$ s. In Fig. S2, we show the magnitudes of the flow velocities at the end of the first beating period, $|\mathbf{u}(\mathbf{x},T)|$, for the variables N, R_{ref}^i and n_{ref}. We consider the flow velocity computed using a certain grid to be converged if $|\mathbf{u}(\mathbf{x},T)|$ at the three sample points are within 5% of those at the finest grid. For all three points, we find that the flow velocities are converged at $N = 20$, $n_{\text{ref}} = 3$ and $R_{\text{ref}}^i = 4$.

Validation of numerical model

We validate our numerical model by comparing the time-averaged feeding current with the experiment of Fields and Yen (1997). The experiment tethered a *Euchaeta rimana* female (L_{b} = 2.5 mm), and traced the time-dependent positions of 20 μm polystyrene beads entrained in the feeding current. The trajectories of the beads and spatial distribution of the magnitude of the feeding current at the antennule region are shown in figs. 3 and 4 of Fields and Yen (1997),

respectively. The beating frequency of the feeding appendages is not reported but we estimate it to be 33 Hz based on the linear regression of the limb paddling frequency during cruise swimming (see figs. 3 and 4 of Svetlichny et al. (2020)).

In Fig. S3, we show the oscillatory nature of the feeding current, $\mathbf{u}(\mathbf{x},t)$, by plotting it (in the absence of prey) in a plane coincident with the centerlines of the antennule at 5 selected time frames during the N-th beating stroke.

We decompose the feeding current during one beating stroke into time-averaged and oscillatory components,

$$\mathbf{u}(\mathbf{x},t) = \mathbf{u}_{\text{avg}}(\mathbf{x}, NT) + \mathbf{u}_{\text{osc}}(\mathbf{x},t), \tag{S5}$$

where $\mathbf{u}_{\text{avg}} = (1/T)\int_{(N-1)T}^{NT} \mathbf{u}\mathrm{d}t$ is the time-averaged feeding current at the N-th beating stroke, and $\mathbf{u}_{\text{osc}}$ represents the oscillatory velocity component of the feeding current. In Fig. S4a, we plot the time-averaged feeding current in our model, and find it is similar to that in fig. 3 of Fields and Yen (1997), in which the flow contracts before reaching the copepod body, and diverges after passing through. The flow pattern is similar to that due to a Stokeslet, which is consistent with the prediction of Visser (2001) and measurements in Malkiel et al. (2003) and Catton et al. (2007). The largest average velocity is around the feeding appendages, and it decays as the distance from the copepod increases. The average velocity shows two local maxima (1.8 mm/s) in front of the proximal region of the antennule, and becomes significantly smaller in the distal region of the antennule (0.15 mm/s). In comparison, experiments reported average velocities at the proximal and distal regions of the antennule are 8 mm/s and 1 mm/s, respectively (see fig. 4 of Fields and Yen (1997)). The experimental velocities are expected to be larger than our numerical velocities, since *Euchaeta rimana* (L_b = 2.5 mm) is larger than our model copepod (L_b = 1mm), and velocity scale is set by the product of the prosome length L_b and beating frequency f.

If we normalize the experimental and numerical velocities by this quantity ($L_b f$), the experimental velocities at the proximal and distal of the antennule are of the same order of magnitude, but about 1.6 and 2.4 times larger than the corresponding numerical values, respectively. Note that we chose the enlarged effective radii of the feeding appendages to make these normalized velocities as close as possible. We attribute the errors in the calculated feeding current to the approximations made in our numerical model: first, the feeding appendage geometries and motion may not be captured accurately, second, we assumed that the antennae are motionless, and third, the use of effective radii for appendages instead of modeling the fine structure of setae and setules on the appendages. In Fig. S4b, we plot the peak-to-peak magnitude of the oscillatory component of the feeding current without the presence of the prey, which is defined as the difference between the two extrema of the magnitude of the feeding current in one beating cycle.

Steady state test

We evaluate the feeding current velocities at the three sample points to estimate how many beating cycles are required for the bending flows across the setae to reach 98% of the steady state value. We first consider the feeding current velocity without the presence of the prey, $|\mathbf{u}(\mathbf{x},t)|$, at Point D. The solid line in Fig. S5a plots the magnitude of its time-averaged velocity component over the first 100 beating cycles, while the vertical bar represents the range of the oscillatory velocity component. We find that the time-averaged feeding current at Point D requires 4 beating cycles to reach 98% of its steady state value. In Fig. S5b (Fig. S5c), we show the magnitudes of the feeding current at the tips of the proximal (distal) setae. The solid line in each panel represents the corresponding time-averaged velocity component, while the vertical bar represents the range of oscillation. We find that it requires the time-averaged feeding current

about 4 and 57 beating cycles for the flow across the proximal and distal setae to reach 98% of their corresponding steady-state values, respectively. This is due to the fact that the feeding current takes longer time to reach steady state at larger distances from the feeding appendages. Therefore, we use the feeding current at $t/T = 60$ to evaluate the steady-state bending flows at all setae on the antennule and feeding appendages.

Bending Flow across the Setae on the Antennule without the Presence of the Prey

In Fig. S6, we plot the x, y and z components of the steady-state $\Delta\mathbf{u}(s,t)$ across the distal and proximal setae on the antennule at selected times over one beating cycle. It is apparent that the bending flow across these setae is highly oscillatory, which are generated by oscillatory movement of the feeding appendages.

Oscillatory component of the bending flow

In Fig. S7a (Fig. S7b), we plot the oscillatory component of the bending flow, $\Delta\mathbf{u}_{osc}(s,t)$, across the distal (proximal) seta at the number of beating cycle when the free-floating prey initiated from Point B (Point C) is generates the largest time-averaged feeding current.

Numerical scheme for setal deformation

We define the physical coordinate of the setal centerline to be $\mathbf{X}(s,t)$, where s is a Langrangian parameter along the centerline of the seta starting from the setal root; L_{seta} is the setal length. Our numerical scheme discretizes the centerline of the seta into M rigid segments with equal arclength $\Delta s = L_{seta}/M$. We express the centerline coordinate of the m-th segment center as $s_{m+1/2} = (m + 1/2)\Delta s$ and the segment endpoints as $s_m = m\Delta s$ and $s_{m+1} = (m + 1)\Delta s$, for $m = 0, 1, \ldots, M - 1$. In the discretized form, we use $\mathbf{X}_m$ and $\mathbf{X}_{m+1/2}$ to represent the physical

coordinate of the setal centerline at the corresponding *m*-th segment endpoint or center, respectively.

Method of regularized Stokeslets

Our implementation of the method of regularized Stokeslets (MRS) is similar to that described in Hyon et al. (2012) and Martindale et al. (2016). We place a total number of N regularized Stokeslets uniformly on the surface of the seta. To do so, we first divide each segment by equally spaced circular cross sections of radius r_{seta}. For each cross section, we place a total number of P regularized Stokeslets equally spaced along the perimeter of each cross section such that the arc distance between successive regularized Stokeslets $2\pi r_{seta}/P$ is approximately the same is the distance between successive cross sections (see Fig. 8). The regularized Stokeslets in the successive cross sections are staggered in such a way that the successive cross sections are rotated around the centerline axis by an angle of π/P. After rotation, the physical coordinates of the regularized stokeslets are denoted by X_n, for $n = 1, 2, \ldots, N$.

We apply the MRS to explicitly evaluate the velocity at the *m*-th segment center, $\mathbf{v}_{m+1/2} = \mathbf{v}(\mathbf{X}_{m+1/2},t)$, which is a sum of the velocity due to the background flow and that due to a linear superposition of the forces due to the regularized Stokeslets:

$$\mathbf{v}_{m+1/2} = \Delta\mathbf{u}(\mathbf{X}_{m+1/2},t) + \sum_{n=0}^{N} S\left(\mathbf{X}_{m+1/2}, X_n, \grave{o}\right) F_n\left(t\right), \tag{S6}$$

where $\Delta\mathbf{u}$ is the bending flow velocity obtained from IBAMR with reference to that at the setal root, F_n is the regularized Stokeslet force centered at X_n at time t, $S\left(\mathbf{X}_{m+1/2}, X_n, \grave{o}\right)$ is the regularized Stokeslet kernel given by Eq. 10(b) in the work of Cortez et al. (2005), and $\grave{o}$ is the regularization parameter which is in the same order of magnitude as $2\pi r_{seta}/P$.

Inextensible Kirchhoff rod theory

Our implementation of the inextensible Kirchhoff Rod Theory (KRT) is similar to that described in Jabbarzadeh and Fu (2020). The inextensible constraint imposed on the seta enforces zero longitudinal deformation of the seta, which implies that

$$\left|\partial_s \mathbf{X}\right| = 1. \tag{S7}$$

This is implemented in our numerical model by assuming all setal segments are all rigid; the transverse deformation of the seta is captured by the angular displacements of the torsional springs connecting adjacent segments (see Fig. S8).

To solve for the internal force and torque exerted on the seta, we first express the hydrodynamic force and torque per length exerted at the setal centerline, denoted by $\mathbf{f}(s,t)$ and $\mathbf{n}(s,t)$ in Eqs. 2 and 3 in the main text, in terms of F_n. In discretized form, we have

$$\mathbf{f}_{m+1/2} = \frac{1}{\Delta s} \sum_{n=m\mathrm{N}/M+1}^{(m+1)\mathrm{N}/M} \mathrm{F}_n \,, \tag{S8}$$

$$\mathbf{n}_{m+1/2} = \frac{1}{\Delta s} \sum_{n=m\mathrm{N}/M+1}^{(m+1)\mathrm{N}/M} \left(\mathrm{X}_n - \mathbf{X}_{m+1/2}\right) \times \mathrm{F}_n \,, \tag{S9}$$

where $\mathbf{f}_{m+1/2} = \mathbf{f}(\mathbf{X}_{m+1/2},t)$ and $\mathbf{n}_{m+1/2} = \mathbf{n}(\mathbf{X}_{m+1/2},t)$ represents the force and torque per unit length at the m-th segment center, respectively. We further use a set of orthonormal basis vectors, $\mathbf{d}_i(\underline{s},t) \in \mathbb{R}^3$ for i = 1, 2, 3, to express the orientation of the setal centerline, and to further relate it with torsion of the cross sections. The unit tangential vector along the setal centerline can be expressed as

$$\mathbf{d}_3 = \partial_s \mathbf{X} \big/ \left|\partial_s \mathbf{X}\right|. \tag{S10}$$

This allows us to use the discretized form of the Kirchhoff Rod equations (Eqs. 2 and 3 in the main text) to further relate $\mathbf{f}_{m+1/2}$ and $\mathbf{n}_{m+1/2}$ with the internal force and torque at the segment ends by using

$$\mathbf{F}_m = \left(\mathbf{f}_{m-1/2} - \mathbf{f}_{m+1/2}\right)\Delta s\,, \tag{S11}$$

$$\mathbf{N}_m = \left(\mathbf{n}_{m-1/2} - \mathbf{n}_{m+1/2}\right)\Delta s - \left(\mathbf{d}_{m-1/2,3}\times\mathbf{f}_{m-1/2} + \mathbf{d}_{m+1/2,3}\times\mathbf{f}_{m+1/2}\right)\Delta s^2/2\,, \tag{S12}$$

where

$$\mathbf{F}_m = \sum_{i=1}^{3} F_{m,i}\mathbf{d}_{m,i}\,, \tag{S13}$$

$$\mathbf{f}_{m\pm1/2} = \sum_{i=1}^{3} f_{m\pm1/2,i}\mathbf{d}_{m\pm1/2,i}\,, \tag{S14}$$

$$\mathbf{N}_m = \sum_{i=1}^{3} N_{m,i}\mathbf{d}_{m,i}\,, \tag{S15}$$

$$\mathbf{n}_{m\pm1/2} = \sum_{i=1}^{3} n_{m\pm1/2,i}\mathbf{d}_{m\pm1/2,i}\,. \tag{S16}$$

We then use the rigid body constraint to express the velocities of the material points on the setal surface, $\mathbf{v}_n = \mathbf{v}(\mathrm{X}_n, t)$, in terms of the translational and rotational velocities at the *m*-th segment,

$$\mathbf{v}_n = \mathbf{V}_{m+1/2} + \boldsymbol{\Omega}_{m+1/2}\times\left(\mathrm{X}_n - \mathbf{X}_{m+1/2}\right), \tag{S17}$$

for $m\mathrm{N}/M + 1 \le n \le (m+1)\,\mathrm{N}/M$. We further express $\boldsymbol{\Omega}_{m+1/2}$ in terms of $\boldsymbol{\Omega}_{1/2}$ and $\mathbf{V}_{m+1/2}$. To do so, we substitute Eq. (S7) into Eq. (S10), and differentiate the latter with respect to time, leading to

$$\frac{\partial\mathbf{V}(s,t)}{\partial s} = \boldsymbol{\Omega}(s,t)\times\mathbf{d}_3(s,t)\,. \tag{S18}$$

The discretized form of Eq. (S18) allows us to use

$$\mathbf{V}_{m+1} - \mathbf{V}_m = \boldsymbol{\Omega}_{m+1/2}\times\left(\mathbf{X}_{m+1} - \mathbf{X}_m\right) \tag{S19}$$

to relate $\boldsymbol{\Omega}_{m+1/2}$ to the difference in the velocities between the two endpoints of the *m*-th segment, and

$$\mathbf{V}_{m\pm1/2} - \mathbf{V}_m = \mathbf{\Omega}_{m+1/2} \times \left(\mathbf{X}_{m\pm1/2} - \mathbf{X}_m \right) \tag{S20}$$

to relate $\mathbf{\Omega}_{m+1/2}$ to the difference in the velocities between the m-th segment center and either endpoint.

Forward time scheme

We adopt a forward time scheme, which utilizes the setal shape and orientation at the time step $t = i\Delta t$, for $i = 0, 1, 2, \ldots$, to solve for centerline velocity of the seta, and then update the setal shape at the following time step $t = (i + 1)\Delta t$.

To do so, we first find the hydrodynamic torque, $\mathbf{N}_1, \mathbf{N}_2, \ldots, \mathbf{N}_{M-1}$, based on the setal shape at the current time step, $t = i\Delta t$. This can be achieved by applying the discretized form of the constitutive equation for the Kirchhoff rod model (Eqs. 4 to 6 in the main text):

$$N_{m,1} = EI \left(\frac{\mathbf{d}_{m+1/2,2} - \mathbf{d}_{m-1/2,2}}{\Delta s} \cdot \mathbf{d}_{m,3} \right), \tag{S21}$$

$$N_{m,2} = EI \left(\frac{\mathbf{d}_{m+1/2,3} - \mathbf{d}_{m-1/2,3}}{\Delta s} \cdot \mathbf{d}_{m,1} \right), \tag{S22}$$

$$N_{m,3} = GJ \left(\frac{\mathbf{d}_{m+1/2,1} - \mathbf{d}_{m-1/2,1}}{\Delta s} \cdot \mathbf{d}_{m,2} \right), \tag{S23}$$

where E is the Young's modulus; $I = \pi r_{\text{seta}}^4/4$ and $J = \pi r_{\text{seta}}^4/2$ are the planar and polar second moment of the seta, respectively. The bending modulus $G = E/[2(1 + \upsilon)]$, where the Poisson's ratio υ is assumed to be 0.3.

Second, we couple the MRS and KRT and solve Eqs. (S6), (S8), (S9), (S11), (S12), (S17), (S19) and (S20) as a linear system by using the internal torque $\mathbf{N}_m$ obtained from Eqs. (S21) to (S23) and the boundary conditions that the setal root is stationary and clamped ($\mathbf{V}_{1/2} = \mathbf{\Omega}_{1/2} = \mathbf{0}$) and the setal tip is force- and moment-free ($\mathbf{F}_M = \mathbf{N}_M = \mathbf{0}$) into the linear system. This allows us

to obtain the force and torque at the setal root, $\mathbf{F}_0$ and $\mathbf{N}_0$, and the translational and rotational velocities at the segment centers, $\mathbf{V}_{m+1/2}$ and $\mathbf{\Omega}_{m+1/2}$.

Last, we update the setal shape and orientation at the following time step, $t = (i + 1)\Delta t$, by using

$$\mathbf{X}_{m+1/2}^{j+1} = \mathbf{X}_{m+1/2}^{j} + \mathbf{V}_{m+1/2}^{j}\Delta t\,, \tag{S24}$$

$$\mathbf{d}_{m+1/2,i}^{j+1} = R\left(\frac{\mathbf{\Omega}_{m+1/2}^{j}}{\left|\mathbf{\Omega}_{m+1/2}^{j}\right|},\ \left|\mathbf{\Omega}_{m+1/2}^{j}\right|\Delta t\right)\mathbf{d}_{m+1/2,i}^{j}\,, \tag{S25}$$

where $R(\mathbf{e},\theta)$ is the rotational matrix that depends on the rotational axis $\mathbf{e}$ and rotational angle θ. $R(\mathbf{e},\theta)$ is explicitly given by Eq. 36 in the work of Olson et al. (2013), and expressed as

$$R(\mathbf{e},\theta) = (\cos\theta)I + (1-\cos\theta)\mathbf{e}\mathbf{e}^{T} + (\sin\theta)(\mathbf{e}\times)\,, \tag{S26}$$

where $I \in \mathbb{R}^{3\times 3}$ is an identity matrix, and for any vector $\mathbf{d}$, $(\mathbf{e}\times)\mathbf{d} = \mathbf{e}\times\mathbf{d}$. The orthonormal basis vectors at the segment endpoints are updated in such a way that

$$\mathbf{d}_{m,i} = \begin{cases} \mathbf{d}_{1/2,i}, & \text{if } m = 0 \\ \mathbf{d}_{M-1/2,i}, & \text{if } m = M \\ \sqrt{\mathbf{A}}\mathbf{d}_{m-1/2,i}, & \text{if } m = 1, 2, ..., M-1 \end{cases}, \tag{S27}$$

where $\mathbf{A} = \sum_{i=1}^{3}\mathbf{d}_{m+1/2,i}\left(\mathbf{d}_{m-1/2,i}\right)^{T}$, and $\sqrt{\mathbf{A}}$ is the square root of $\mathbf{A}$.

A convergence test was performed on a seta of length L_{seta} = 200 μm, radius r_{seta} = 1 μm and Young's modulus E = 10^7 N/m^2, which is subjected to a background shear flow $\Delta\mathbf{u} = \dot{\varepsilon}s\mathbf{d}_{0,2}\sin(2\pi ft)$, where the frequency f = 30 Hz, and the shear rate $\dot{\varepsilon}$ = 1 s^{-1}. We note that the parts that take most runtime in each time step are the linear solves implied by the matrix inverse of the regularized Stokeslet kernel, $\sum_{i=0}^{\mathrm{N}}\mathrm{S}\left(\mathbf{X}_{m+1/2},\mathrm{X}_i,\grave{\mathrm{o}}\right)$, as shown in Eq. (S6). Here we adopt the numerical framework that is stated in the "partial updating of hydrodynamic interaction"

section in Jabbarzadeh and Fu (2020). In short, the kernel is recalculated only if the maximum difference between $\mathbf{X}^{j}$ and $\mathbf{X}^{j'}$ is larger than a prescribed threshold,

$$\max\left(\left|\mathbf{X}^{j}-\mathbf{X}^{j'}\right|\right) > Cr_{\text{seta}}, \tag{S28}$$

where $\mathbf{X}^{j'}$ represents the setal displacement at last time step that the kernel is updated, and C is a dimensionless constant to be determined in the convergence test. We set the setal deformation to be convergent if the maximum difference in the setal root curvature at selected (M, Δt, C) and the finest discretization level used in our numerics (M = 100, $\Delta t = 4 \times 10^{-7}/f$, $C = 4 \times 10^{-4}$) is less than 5%. The convergence test results show that for $\delta = 2\pi r_{\text{seta}}/(3P)$ and P = 12, the magnitude of the root curvature converges when $\Delta t = 2 \times 10^{-6}/f$ and C = 0.4.

Reference

Bhalla, A. P. S., R. Bale, B. E. Griffith, and N. A. Patankar. 2013. A unified mathematical framework and an adaptive numerical method for fluid–structure interaction with rigid, deforming, and elastic bodies. J. Comput. Phys. **250:** 446–476.

Catton, K. B., D. R. Webster, J. Brown, and J. Yen. 2007. Quantitative analysis of tethered and free-swimming copepodid flow fields. J. Exp. Biol. **210:** 299-310.

Conway, D. V. P. 2006. Identification of the copepodite developmental stages of twenty-six North Atlantic copepods. Marine Biological Association of the United Kingdom.

Cortez, R., L. Fauci, and A. Medovikov. 2005. The method of regularized Stokeslets in three dimensions: analysis, validation, and application to helical swimming. Phys. Fluids **17:** 031504.

Fields, D. M., and J. Yen. 1997. Implications of the feeding current structure of *Euchaeta rimana*, a carnivorous pelagic copepod, on the spatial orientation of their prey. J. Plankton Res. **19:** 79-95.

Gill, C. W., and S. A. Poulet. 1986. Utilization of a computerized micro-impedance system for studying the activity of copepod appendages. J. Exp. Mar. Biol. Ecol. **101:** 193-198.

Hyon, Y., Marcos, T. R. Powers, R. Stocker, and H. C. Fu. 2012. The wiggling trajectories of bacteria. J. Fluid Mech. **705:** 58–76.

Jabbarzadeh, M., and H. C. Fu. 2020. A numerical method for inextensible elastic filaments in viscous fluids. J. Comput. Phys. **418:** 109643.

Koehl, M. A. R., and J. R. Strickler. 1981. Copepod feeding currents: food capture at low Reynolds number. Limnol. Oceanogr. **26:** 1062-1073.

Malkiel, E., J. Sheng, J. Katz, and J. R. Strickler. 2003. Digital holography of the flow field generated by a feeding calanoid copepod, *Diaptomus minutus*. J. Exp. Biol. **206:** 3657-3666.

Martindale, J. D., M. Jabbarzadeh, and H. C. Fu. 2016. Choice of computational method for swimming and pumping with nonslender helical filaments at low Reynolds number. Phys. Fluids **28:** 021901.

Olson, S. D., S. Lim, and R. Cortez. 2013. Modeling the dynamics of an elastic rod with intrinsic curvature and twist using a regularized stokes formulation. J. Comput. Phys. **238:** 169–187.

Peskin, C. S. 1972. Flow patterns around heart valves: a numerical method. J. comput. phys. **10:** 252–271.

---. 2002. The immersed boundary method. Acta Numer. **11:** 479–517.

315 Svetlichny, L., P. S. Larsen, and T. Kiørboe. 2020. Kinematic and dynamic scaling of copepod
316 swimming. Fluids **5:** 68.
317 Tiselius, P., E. Saiz, and T. Kiørboe. 2013. Sensory capabilities and food capture of two small
318 copepods, *Paracalanus parvus* and *Pseudocalanus* sp. Limnol. Oceanogr. **58:** 1657-1666.
319 van Duren, L. A., and J. J. Videler. 2003. Escape from viscosity: the kinematics and
320 hydrodynamics of copepod foraging and escape swimming. J. Exp. Biol. **206:** 269-279.
321 Visser, A. W. 2001. Hydromechanical signals in the plankton. Mar. Ecol. Prog. Ser. **222:** 1-24.

322

Table S1. Hydrodynamic characteristics of the cephalic appendages – antennules (A1), antennae (A2), mandibles (Md), first maxillae (Mx1), and maxillipeds (Mxp) – of copepod model

Appendage	Root diameter (mm)[a]	Tip diameter (mm)[b]	*l* (mm)	*w* (mm)	Segment	Length (mm)[c]	α (deg)[d]		Angle (rad)[e]
							endopod	exopod	
A1	0.062	0.022	0.051	0.031	–	1.097	–		–
A2	0.076	0.101	0.181	0.077	Proximal	0.184	36	64	$\theta_1 = +0.449 + 0.614\cos(2\pi ft - 2.351)$
					Distal	0.152	–	–	$\theta_2 = -0.217 + 0.656\cos(2\pi ft + 2.900)$
Md[f]	0.070	0.093	0.269	0.070	Proximal	0.111	80		$\theta_1 = +0.344 + 0.581\cos(2\pi ft - 1.410)$
					Distal	0.162	–		$\theta_2 = -0.307 + 0.640\cos(2\pi ft - 1.772)$
Mx1	0.050	0.050	0.319	0.066	–	0.179	10		$\theta_1 = +0.361 + 0.527\cos(2\pi ft - 0.724)$
Mxp	0.064	0.085	0.476	0.053	Proximal	0.223	21		$\theta_1 = +0.094 + 0.328\cos(2\pi ft + 0.876)$
					Distal	0.157	–		$\theta_2 = -5.267 + 0.527\cos(2\pi ft + 1.171)$

[a] The diameter of appendage at its most proximal cross-section.

[b] The diameter of appendage at its most distal cross-section.

[c] The axial length (true length) of the appendage segment.

[d] Positive α follows the arrow direction in Fig. S1a inset.

[e] The "Angle" represents θ_1 and θ_2 in Fig. S1a inset for proximal and distal segments, respectively; f is the beating frequency; t is the time. Positive θ_1 and θ_2 follow the arrow directions in Fig. 1a inset.

[f] The biramous Md is simplified to be uniramous (single branch) with a distal segment attached to a proximal segment.

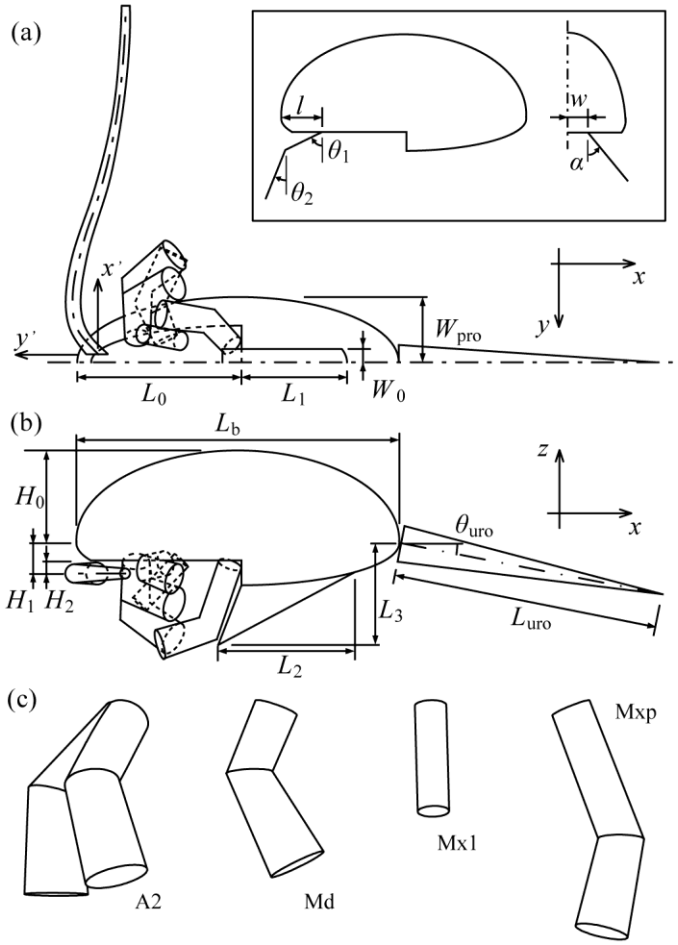

Fig. S1. (a) Ventral-dorsal and (b) lateral views of the feeding-current feeding copepod model. The cone-shaped urosome is attached to the prosome composing of two semi-ellipsoids. The ventral semi-ellipsoid is extruded for the attachment of cephalic appendages which from left to right are the antennules (A1), antennae, mandibles, first maxillae, and maxillipeds. The swimming legs are modeled as a prism intersecting with the prosome. (c) The schematics of the four feeding appendages in our model. The antenna is treated as two separated branches, mandible, first maxilla and maxilliped as one branch. The left and right insets are schematics illustrating the position of the attachment point [l, w], longitudinal angular displacement [θ_1, θ_2], and lateral angular displacement α, of the cephalic appendages. The coordinate of the A1

centerline in the body-fixed frame is defined by $y' = 1.704(x')^5 - 5.739(x')^4 + 7.519(x')^3 - 4.550(x')^2 + 0.967x'$, where both x' and y' are in units of mm. The prosome height is 0.399 mm, the base diameter of urosome is 0.097 mm and the other dimensions are: L_b = 1.000 mm, L_{uro} = 0.840 mm, L_0 = 0.505 mm, L_1 = 0.344 mm, L_2 = 0.409 mm, L_3 = 0.301c W_b = 0.200 mm, W_0 = 0.045 mm, H_0 = 0.278 mm, H_1 = 0.090 mm, H_2 = 0.031 mm and θ_{uro} = 0.190 rad.

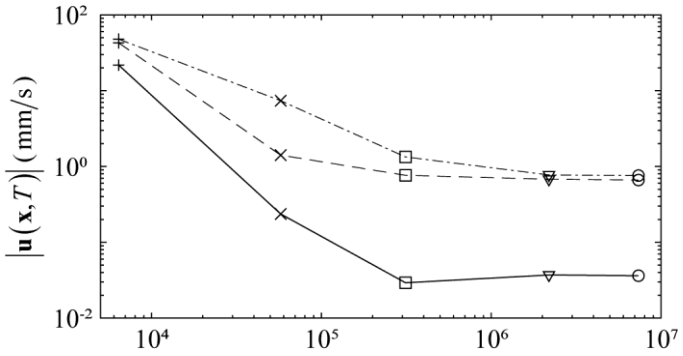

Fig. S2. Magnitude of the feeding current velocity $|\mathbf{u}(\mathbf{x}, t)|$ as a function of the total number of grid points at the end of the first beating period, $t = T$. The solid, dashed, dash-dotted and dotted lines represent the velocity at the distal setal tip, proximal setal tip, and Point D, respectively. The plus (+) symbols denote the number of grids when the number of coarsest grids per length $N = 20$ and there is no mesh refinement. The cross (×) symbols denote $N = 20$, refinement level $n_{\text{ref}} = 1$ and refinement ratio $R^1_{\text{ref}} = 4$. The square (□) symbols denote $N = 20$, $n_{\text{ref}} = 2$, $R^1_{\text{ref}} = R^2_{\text{ref}} = 4$. The triangle (▽) symbols denote $N = 20$, $n_{\text{ref}} = 3$, $R^1_{\text{ref}} = R^2_{\text{ref}} = R^3_{\text{ref}} = 4$. The circle (○) symbols denote $N = 20$, $n_{\text{ref}} = 5$, $R^1_{\text{ref}} = R^2_{\text{ref}} = R^3_{\text{ref}} = 4$ and $R^4_{\text{ref}} = 2$.

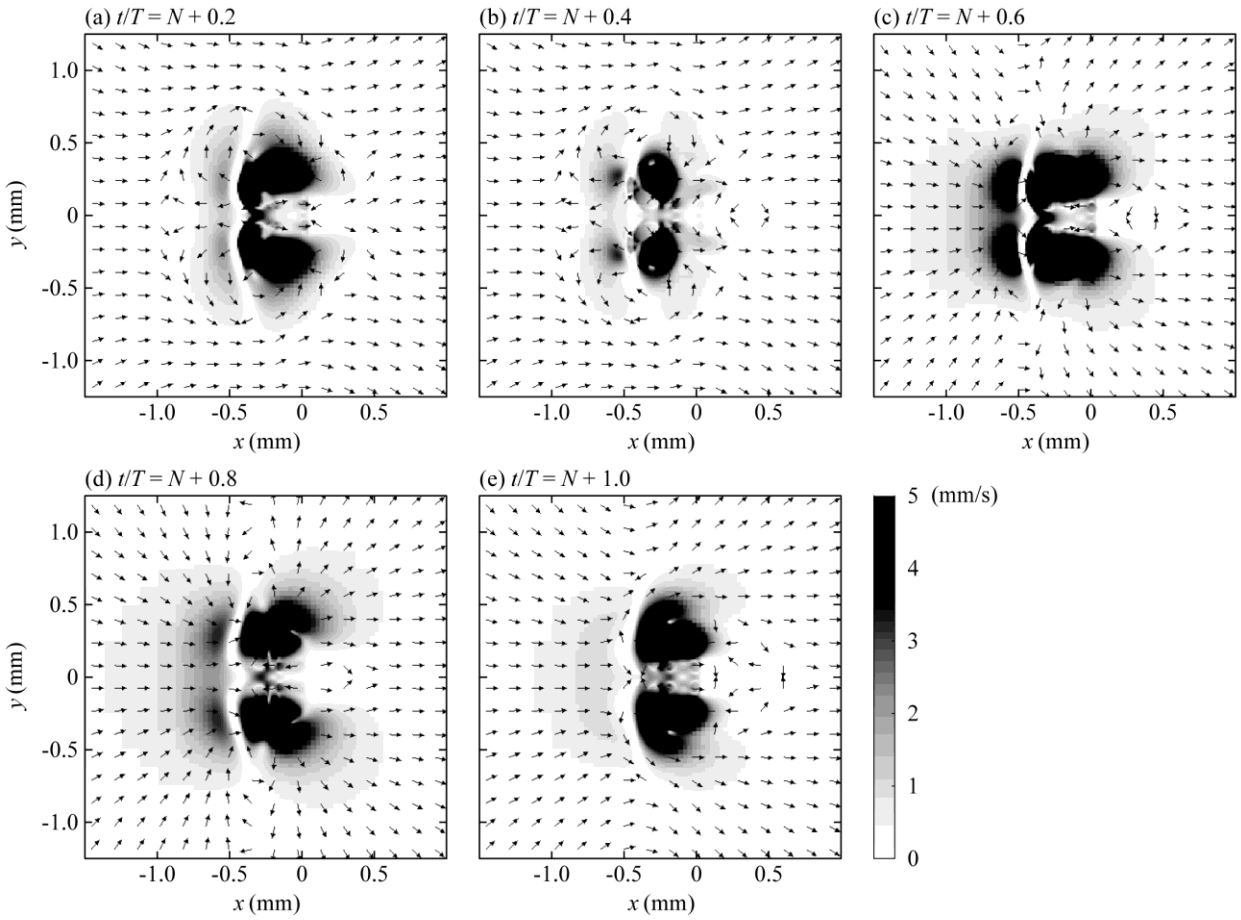

Fig. S3. (a)-(e) Spatial distribution of the instantaneous feeding current without the presence of the prey, $\mathbf{u}(\mathbf{x},t)$, in a plane coincident with the centerlines of the antennules (A1) at 5 selected time frames during the hundredth beating cycle (N = 99). The maximum $|\mathbf{u}(\mathbf{x},t)|$ is limited to 5 mm/s to show the flow pattern around A1. In each panel, the pseudocolor plot shows the magnitude of the feeding current, while the arrows show the direction of the feeding current projected to the visualization plane. The whitest zones indicate the area occupied by A1 and copepod body, while the darkest zones represent the flow around the feeding appendages.

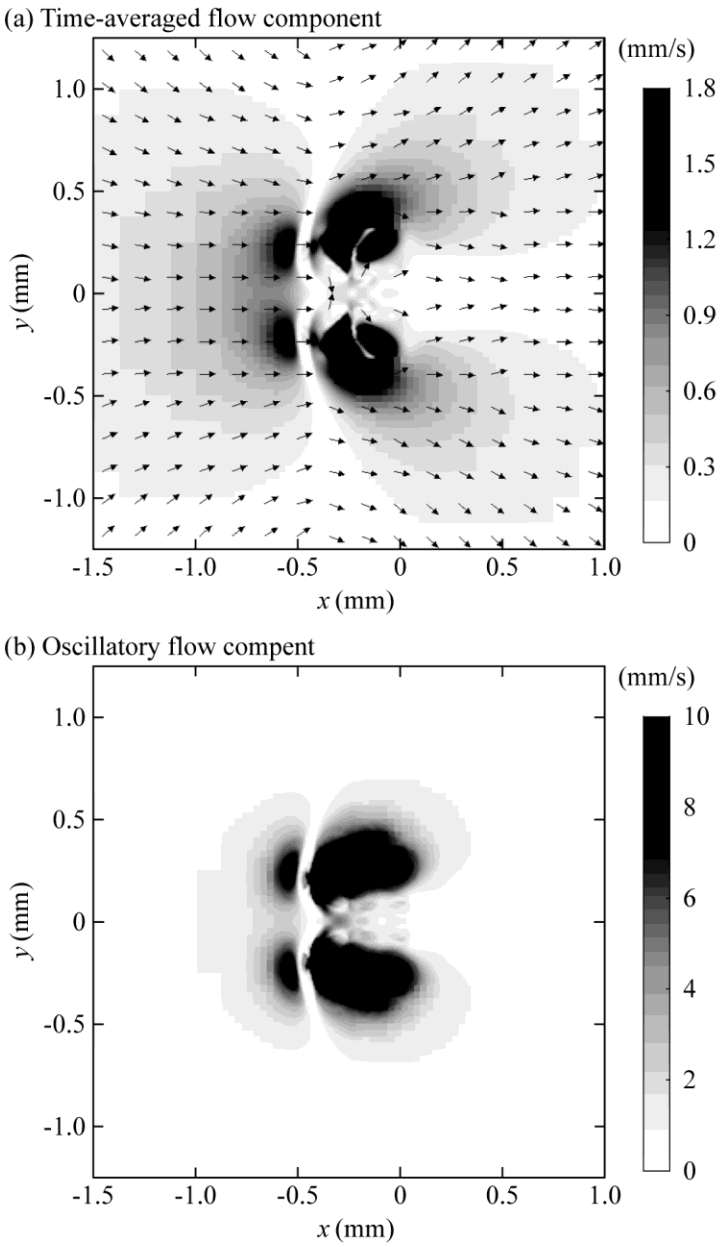

366

367 Fig. S4. (a) Spatial distributions of the feeding current without the presence of the prey averaged
368 over one beating cycle, $\mathbf{u}_{avg}$, in a plane coincident with the centerlines of the antennules (A1).
369 The pseudocolor plot shows the magnitude of the feeding current, while the arrows show the
370 direction of the feeding current projected to the visualization plane. (b) Pseudocolor plot of the
371 peak-to-peak magnitude of the oscillatory component of the feeding current without the presence
372 of the prey in a plane coincident with the A1 centerlines. The maximum magnitudes in panels (a)

373 and (b) are limited to 1.8 mm/s and 10 mm/s, respectively, to show the corresponding flow
374 pattern around A1.

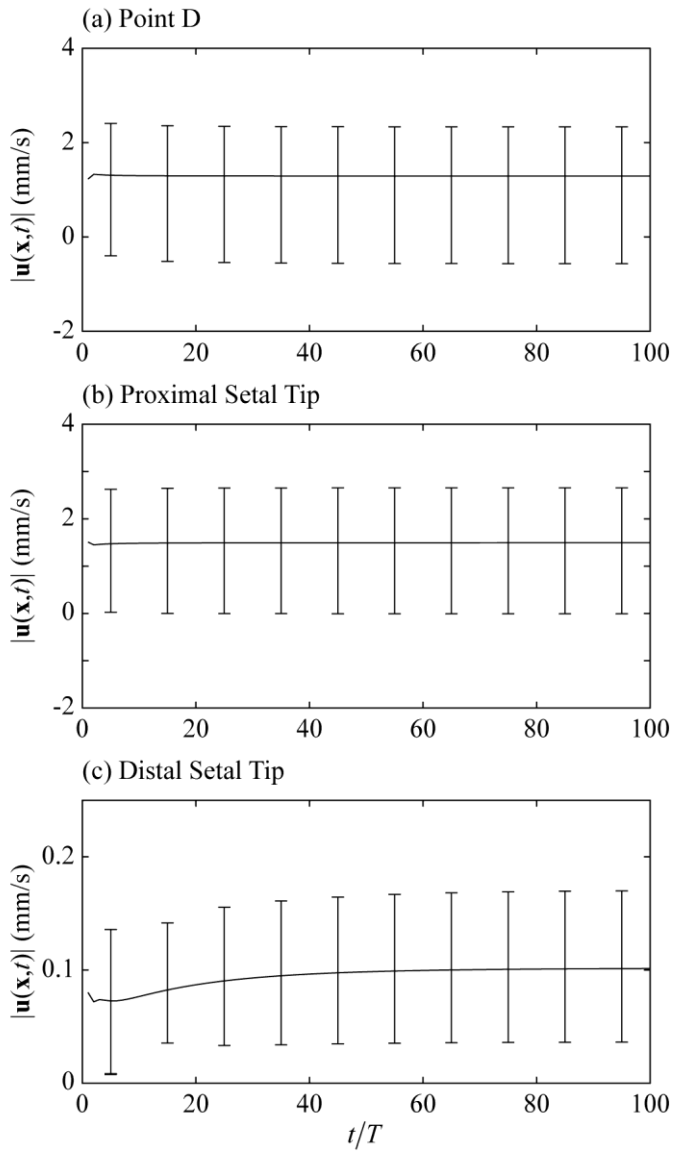

Fig. S5. Magnitude of the feeding current without the presence of the prey, $|\mathbf{u}(\mathbf{x},t)|$, at (a) Point D, the tips of the (b) proximal and (c) distal setae on the antennule as a function of beating cycle. The copepod's feeding appendages are beating at 30 Hz. The solid line in each panel represents the feeding current averaged over one beating cycle, while vertical bars represent the range of the oscillatory component of the feeding current at the selected beating cycles.

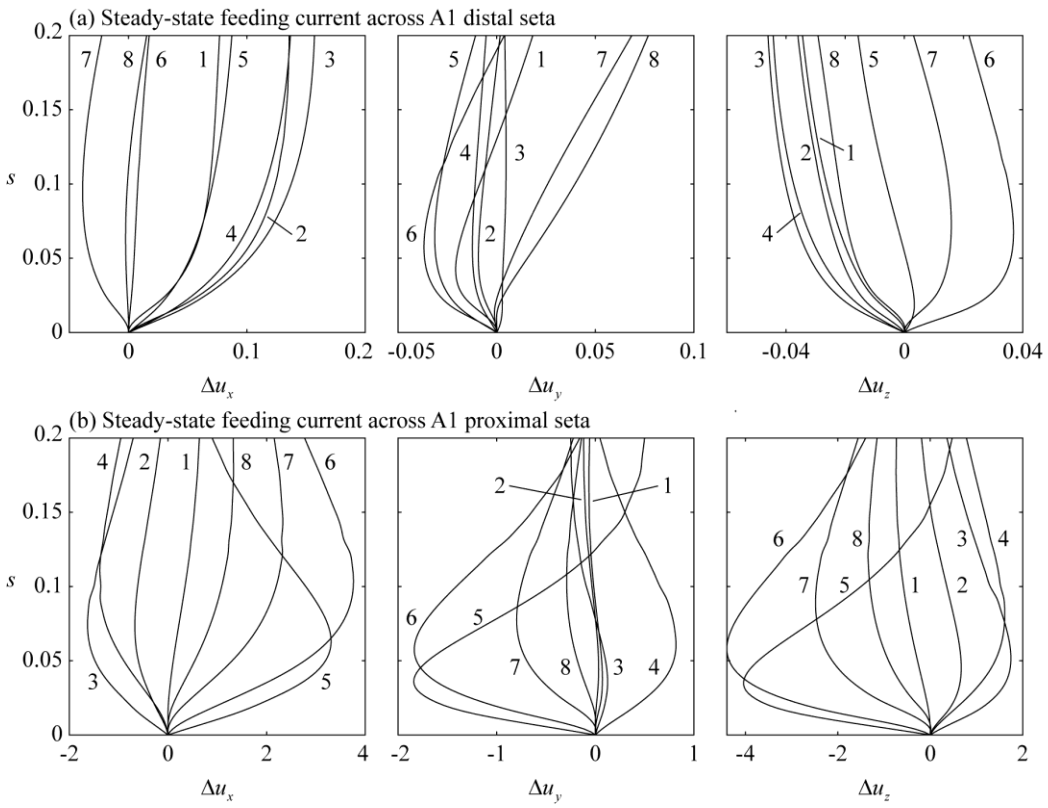

Fig. S6. Instantaneous bending flow, $\Delta\mathbf{u}(s,t)$, across the left (a) distal and (b) proximal setae on the antennule without the presence of prey during one beating cycle, after the bending flow averaged over one beating cycle reaches the steady state. A sequence of $\Delta\mathbf{u}(s,t)$, plotted in terms of its components in the *x*, *y* and *z* direction in units of mm/s, at equally spaced times during one cycle of oscillation is labeled by the numbers 1-8. The arclength along the setal centerline (*s*, units of mm) is measured starting at the setal root.

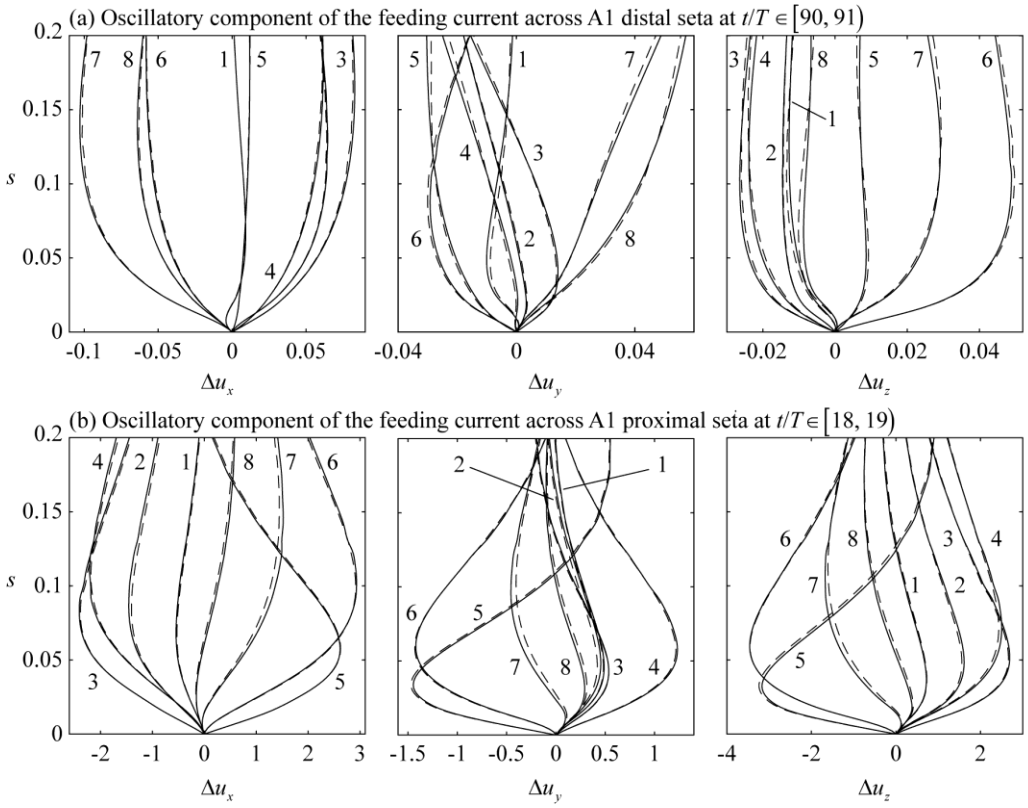

Fig. S7. Oscillatory components of the bending flows, $\Delta\mathbf{u}_{osc}(s,t)$, across the left (a) distal and (b) proximal setae on the antennule in the beating cycle during which the time-averaged bending flow induced by the free-floating prey is the largest across the corresponding seta. A sequence of ~~shapes~~ $\Delta\mathbf{u}_{osc}(s,t)$, plotted in terms of its components in the *x*, *y* and *z* direction in units of mm/s, at equally spaced times during the beating cycle is labeled by the numbers 1-8. The arclength along the setal centerline (*s*, units of mm) is measured starting at the setal root.

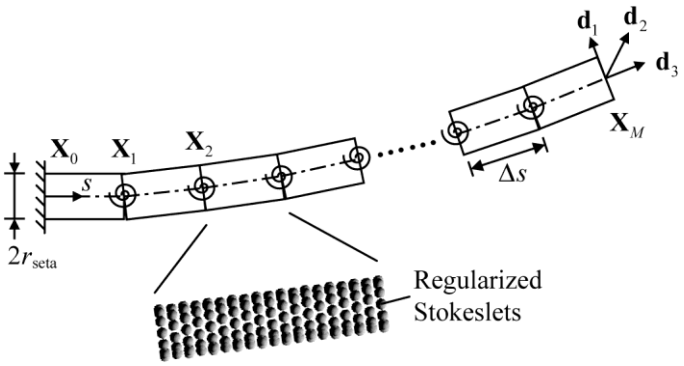

Fig. S8. Schematic of the clamped seta in our numerical model. The arclength of the seta is L_{seta}, and radius r_{seta}. The Lagrangian parameter $s \in [0, L_{\text{seta}}]$ is defined to start from the setal root and along the setal centerline. The three orthogonal vectors, $\mathbf{d}_1$, $\mathbf{d}_2$ and $\mathbf{d}_3$, are to represent the setal orientation, with $\mathbf{d}_3$ along the s direction. The seta is discretized into M segments of equal arc length Δs. The physical centerline coordinates of the two m-th segment nodes are represented by $\mathbf{X}_m$ and $\mathbf{X}_{m+1}$, for $m = 0, 1, \ldots, M - 1$. The regularized Stokeslets are distributed uniformly at the surface of each segment.